Geophysical Research Letters

Ocean Surface Wave-Current Signatures From Satellite Altimeter Measurements

Y. Quilfen[1] iD **and B. Chapron[1]**

[1]IFREMER, University of Brest, CNRS, IRD, Laboratoire d'Océanographie Physique et Spatiale, IUEM, Brest, France

Abstract Ocean currents can strongly impact the propagation of swell systems. Satellite altimetry routinely provides measurements of ocean surface significant wave heights (Hs). A self-consistent space-scale decomposition is applied to Hs measurements obtained from different altimeters. This method helps reveal overlooked statistical properties at scales less than 100 km, where mesoscale and submesoscale upper ocean circulation drives a significant part of the variability in the coupled ocean-atmosphere system. In particular, systematic signatures related to wave-current interactions are clear at global and regional scales. In the Agulhas current system, the proposed space-scale decomposition further reveals organized and persistent patterns. To leading order, the redistribution of swell energy follows the cumulative impact of the large-scale current vorticity field on wave train kinematics. This relationship causes significant swell ray deflection and localized trapping phenomena, which are adequately captured by altimeter measurements.

Plain Language Summary Long and energetic surface waves radiating from distant storms may eventually cover a full ocean basin with a lifetime that can extend over a few weeks. Chances are that these swell fields will propagate over regions characterized by strong ambiant upper ocean currents. Resulting interactions can then trigger sea state variability, including the formation of severe crossing sea conditions. To better document these anticipated effects at global and regional scales, a new methodology is applied to best exploit multisatellite altimeter measurements. As obtained, the resulting augmented data sets provide an unprecedented evidence of the co-variability of surface waves and currents over all ocean basins. More regionally, the analysis shows that persistent and localized sea state anomalies in the Agulhas current region are well explained by swell refraction and focusing effects in the variable current stream. The proposed methodology opens new perspectives for studies and applications combining numerical modeling and satellite observations.

1. Introduction

Interactions between waves and currents have long been studied to explain local sea state changes (Lavrenov & Porubov, 2006; Mallory, 1974). Indeed, currents impact the dispersion of surface waves, and surface current fluctuations can lead to the formation of anomalous large-amplitude waves. Theoretical frameworks can build on ordinary differential equations that describe the kinematics and dynamics of wave train evolution in the presence of surface currents, explaining the cumulative impact of the current vorticity field on wave train kinematics. Ultimately, these impacts can lead to significant ray deflection (Dysthe, 2001; Gallet & Young, 2014; Kenyon, 1971; White & Fornberg, 1998).

Joint analysis of numerical modeling outputs and satellite measurements have confirmed that spatial wave height variations result from these refraction effects (Ardhuin et al., 2017; Kudryavtsev et al., 2017; Quilfen et al., 2018). In Ardhuin et al. (2017), a relationship was proposed that quantitatively related the mesoscale variability in significant wave height (hereafter Hs), predicted by the WAVEWATCH III numerical model, and the statistical distribution of surface currents. Unfortunately, comparisons with altimeter measurements were not fully conclusive for spatial scales below ~80 km. This result was mainly because the mesoscale geophysical variability is often buried within altimeter measurement noise (at scales up to 100 km). To avoid such limitations and better exploit the capabilities of satellite altimeters to provide more robust estimates of the local significant wave height and sea surface height mesoscale variability, Quilfen et al. (2018) considered a novel approach to analyze altimeter measurements. This approach relies on a data analysis methodology called empirical mode decomposition (EMD, Huang et al., 1998; Huang & Wu, 2008), widely applied in other geophysical or biomedical engineering studies. Developed to cope with both nonlinear and

nonstationary processes, EMD often overcomes limitations of other approaches, such as Fourier filtering and/or wavelet-based analysis (Huang et al., 1998; Huang & Wu, 2008). Here this approach is extended to global satellite altimeter measurements to further highlight the striking evidence of large and persistent Hs variability triggered by surface currents.

Section 2 presents the data and the EMD-based approach for the noise filtering and analysis of altimeter measurements, section 3 presents the results, and section 4 contains a summary of the results and discussion.

2. Data and Methods

2.1. Data

We use altimeter data over a 3-year period from 2014 to 2016 when three altimeters provided quality-controlled measurements of Hs and absolute dynamic topography (ADT): (1) the dual-frequency (13.6 GHz in the Ku band, 5.3 GHz in the C band) Jason-2 satellite launched on 20 June 2008, operating with a nominal ground track repeat cycle of 10 days, (2) the Ku band Cryosat-2 satellite launched on 8 April 2013, with a nominal ground track repeat cycle of 369 days, (3) the Ka band (35 GHz) Altika on-board the SARAL satellite launched on 25 February 2013, with a nominal ground track repeat cycle of 35 days. These altimeters perform measurements at nadir along the satellite track, and the standard processing delivers 1-Hz data with a ground sampling that slightly varies from 6 to 7 km depending on the altimeter.

We use quality-controlled, unfiltered and not resampled, along-track ADT data, together with altimeter-gridded products of surface geostrophic currents. The latter are derived from low-pass filtered ADT measurements, which are optimally interpolated to produce mean daily fields at 1/4° resolution (Ducet et al., 2000). These data are provided by the Copernicus Marine Environmental Service (CMEMS, http://marine.copernicus.eu/services-portfolio/access-to-products/). We use quality-controlled, unfiltered and not resampled, along-track Hs measurements provided by the Institut Français de Recherche pour l'Exploitation de la MER (IFREMER; Queffeulou & Croizé-Fillon, 2013, ftp://ftp.ifremer.fr/ifremer/cersat/products/swath/altimeters/waves/). As the data providers for Hs and ADT data are different, the data editing performed before dissemination is different and may impact the estimations of the spectral tails presented hereafter.

2.2. Methods: EMD of Along-Track Altimeter Data

Standard unfiltered ADT and Hs 1 Hz data are noisy at the sensor ground sampling locations. The main sources of noise come from the altimeter waveform retracking algorithms, instrumental noise, and geophysical variability within the altimeter footprint (Dibarboure et al., 2014; Sandwell & Smith, 2005; Thibaut et al., 2010). Analysis of fine-scale ocean dynamics then requires preliminary noise filtering (e.g., Heslop et al., 2017; Morrow et al., 2017). To analyze and filter the altimeter data, we use an approach described in Kopsinis and McLaughlin (2009), the key part of which is the nonparametric EMD (Huang et al., 1998; Wu & Huang, 2004).

EMD is an adaptive method developed to analyze nonlinear and nonstationary processes. It is based on the local characteristic sampling scale of the data and decomposes signals into a finite and often small number of uncorrelated scale-dependent components, called intrinsic mode functions (IMFs, see supporting information, Figure S1). Each IMF satisfies the following properties: (1) The number of zero crossings and the number of extrema must either be equal or differ by zero or by one. (2) The average of upper envelop (joining the IMF maxima) and lower envelop (joining the IMF minima) is zero. These properties enable the estimation of the time-frequency-energy distribution within each IMF through a classical Hilbert transform (Huang & Wu, 2008). IMFs are modulated in amplitude and in frequency, to cope with nonstationarity, and also with strongly nonlinear signals since EMD is based upon detection of the signal extrema. By construction, the EMD method ranks the IMFs from the first one containing the fastest fluctuations to the last one containing the overall trend.

EMD has been used for specific applications, such as biomedical engineering, speech processing, and geophysical studies (e.g., Carmona & Poveda, 2014; Chen et al., 2013, 2017; Wang et al., 2015; Xu et al., 2014), and it also provides a means for efficient signal denoising. Indeed, when applied to a signal containing pure fractional Gaussian noise, EMD acts as a dyadic filter bank. As a consequence, the IMF spectra exhibit self-similarity and the IMF's variance decreases linearly from the first one to the last one (Flandrin et al., 2004). In the EMD basis, the Gaussian noise is colored and its behavior can be estimated from the first
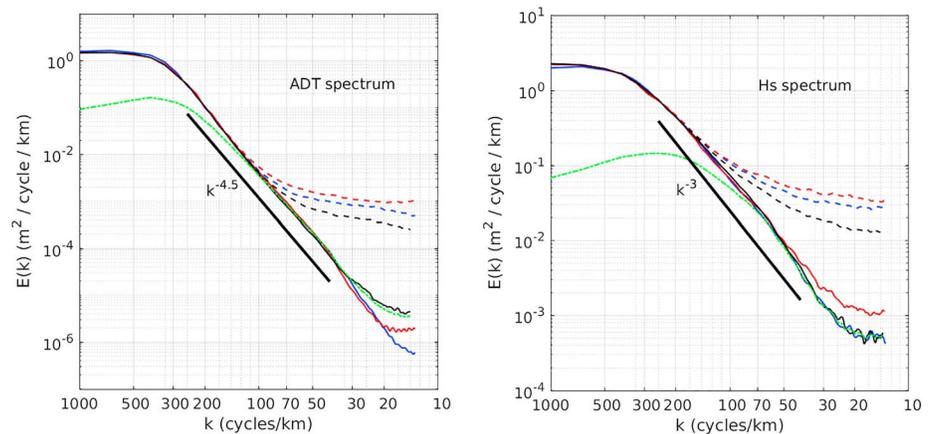
Figure 1. Power spectral density (PSD) as a function of wavenumber (*x* axis labels in kilometer) for altimeter ADT (left) and Hs (right) measurements: SARAL/Altika (black), Cryosat-2 (red), and Jason-2 (blue), time period 2014–2016, Agulhas region. Dashed lines are for raw 1-Hz data and solid lines for filtered data. The first IMF PSD of filtered ADT (left) and Hs (right) is shown as a dashed-dotted green line (these intrinsic mode functions are computed from the three altimeters merged data set). Solid black lines give the $k^{-4.5}$ (left) and k^{-3} (right) dependence between 250 and 40 km of wavelength. ADT = absolute dynamic topography; IMF = intrinsic mode functions.

IMF variance. These properties have been exploited in several studies (e.g., Han & van der Baan, 2015; Kopsinis & McLaughlin, 2009) to develop an EMD-based denoising method using thresholding techniques inspired by wavelet-based denoising methods.

For this study, continuous along-track data segments are first processed, closely following recommendations given by Kopsinis and McLaughlin (2009), as these authors performed a thorough optimization of the method. We use the "clear iterative interval-thresholding" technique that accounts for the fact that the first IMF, containing the highly fluctuating part of the signal, is likely to contain some energetic geophysical signal contributions in addition to noise (see Kopsinis & McLaughlin, 2009, for details).

EMD is particularly relevant because it is a data-driven, self-consistent approach, which does not require a priori hypothesis on the true geophysical signal content. It does not require to be tuned as a function of the ocean basin, for a particular season, or as a function of the different altimeters that have different noise characteristics (see supporting information, Figure S2). A consequence is that it avoids spectral ringing that likely imprints the spectral shape of data denoised with boxcar-like filters and wavelet-based denoising techniques.

Figure 1 shows the ADT and Hs spectra in the Agulhas region, which is known to be a particularly energetic region. The dashed lines show the power spectral density (PSD) of the raw 1-Hz data for the three altimeters. The curves separate for scales slightly less than 100 km, reflecting the different noise levels and showing the scales that are significantly impacted. As expected, the Cryosat-2 raw measurements are noisier because the analysis includes areas where Synthetic Aperture Radar processing is performed (see supporting information, Figure S2). The SARAL/Altika measurements have decreased noise levels due to the high sampling rate used to average the 1-Hz measurements. Applying the EMD-based method, all three curves now exhibit very similar spectral content down to 30 km for ADT and down to 50 km for Hs. At shorter scales, the methodology reaches its inherent limit, as the reference noise level is estimated from the IMF1 mostly associated with these short scales. Embedded geophysical signals cannot be separated from noise if the signal-to-noise ratio (SNR) is too low. Then, it depends on the 1-Hz SNR for each instrument.

For reference, in western boundary currents, Dufau et al. (2016) estimated that the along-track mesoscale resolution capabilities for the SARAL/Altika, Cryosat-2, and Jason-2 altimeters reach 40, 45, and 50 km, respectively. Future improvements in altimeter design and waveform processing will allow these limits to be extended.

Other factors possibly impacting further the method and the derived mean spectral content are as follows: (1) The data editing previously performed for each of the three altimeters. (2) The different true spatial

resolution of the 1-Hz measurements (SARAL/Altika is better than other altimeters). (3) The different locations of ground tracks for each altimeter that likely result in different sampling of the geophysical variability in the Agulhas region, where both surface currents and mesoscale Hs variability are large (see supporting information, Figure S3). (4) The residual errors such as geoid errors.

As shown in Figure 1, the ADT PSD is linear for length scales between 250 and 40 km. Fitted to a $k^{-\alpha}$ law, estimated α values and associated 95% confidence limits are $-4.57\,(\pm0.04)$, $-4.41\,(\pm0.06)$, $-4.50\,(\pm0.04)$, for Saral, Jason-2, and Cryosat-2, respectively. Differences can be attributed partly to the different sampling by each altimeter of the different current patterns within the study area. To estimate the slope scatter for the defined Agulhas region, the α values are estimated for each repeat orbit of the Jason-2 altimeter. As the Jason-2 repeat cycle is short by comparison with the Saral or Cryosat-2 one, PSD from many cycles can be averaged to estimate the slope for one ground track. Eighteen different repeat orbits cross the area and the α standard deviation is 0.26, which is significant relatively to the three altimeters PSD slope differences. For the Hs, the PSD slope does not follow a linear trend but the PSD shape can be compared with a k^{-3} law for length scales between 250 and 40 km. In the range of scales resolved with 1-Hz altimeter measurements, this is close to results reported by Ardhuin et al. (2017) from very high resolution (1/60°) numerical simulations of the WAVEWATCH III model forced with the Regional Ocean Modeling System (ROMS) to model surface currents at 1.5 km.

3. Persistent Basin-Scale Signatures of Waves/Current Interactions

3.1. ADT and Hs Mesoscale Variability Over the Global Ocean

From the conservation of wave action, the spatial variability in Hs results from the propagation dispersion changes. The Hs spatial log-variability closely follows the surface current gradient variability. The global altimeter coverage and the proposed denoised data set make it possible to further analyze this expected covariation down to scales of a few tens of kilometers. Following the data denoising step, a second EMD analysis is performed. The resulting first IMF should then solely contain information related to the geophysical mesoscale variability down to the altimeter sampling capability. The higher-order IMFs will carry information related to very large scale variability and trends. For the Agulhas region, the corresponding spectral content of IMF1 is shown in Figure 1 as green dash-dotted lines. The global distribution of the first IMF variance is shown in Figure 2 for a data set that merges the data from the three altimeters. The variance is computed as the mean of IMF1 squared amplitudes within each grid cell. It then aggregates data from each altimeter whose track intersects the grid cell.

The ADT variance patterns obtained from the filtered data are closely related to the expected location of the main dynamical and/or rich-eddying regions. The global map of the Hs variance clearly demonstrates that large mesoscale variability almost coincides with the ADT variance patterns. This finding provides striking evidence of regional wave/current interactions that shape the sea state variability. Wave/current interaction mechanisms are further analyzed hereafter to give the physical interpretation of this result. A sensitivity study has been conducted to verify that changing the number of altimeters used to map the mean fields does not change significantly the interpretation of the results. For instance, removing Cryosat-2 from the analysis induces differences of order less than 10% in the areas showing the maximum of variance.

Different processes interplay to explain the evolution of the wave field in the presence of currents. As already mentioned, one key effect is the cumulative impact of the current vorticity field on wave train kinematics to ultimately cause significant ray deflection. The advection of wave action by the current vector and local modification of the wind vector and associated stress relative to the current vector must also be considered. In the case of a swell train, refraction and advection are the main processes that contribute to the evolution of the wavefield (Ardhuin et al., 2017; Irvine & Tilley, 1988).

Modeling the propagation and transformation of a swell train through a variable current field can be done as described in Dysthe (2001) or Kudryavtsev et al. (2017). The main assumptions are that the swell does not dissipate as it travels through the current system (time scaling) and that the current itself is time-independent during swell propagation. Equations for the wave train evolution can be written as follows:
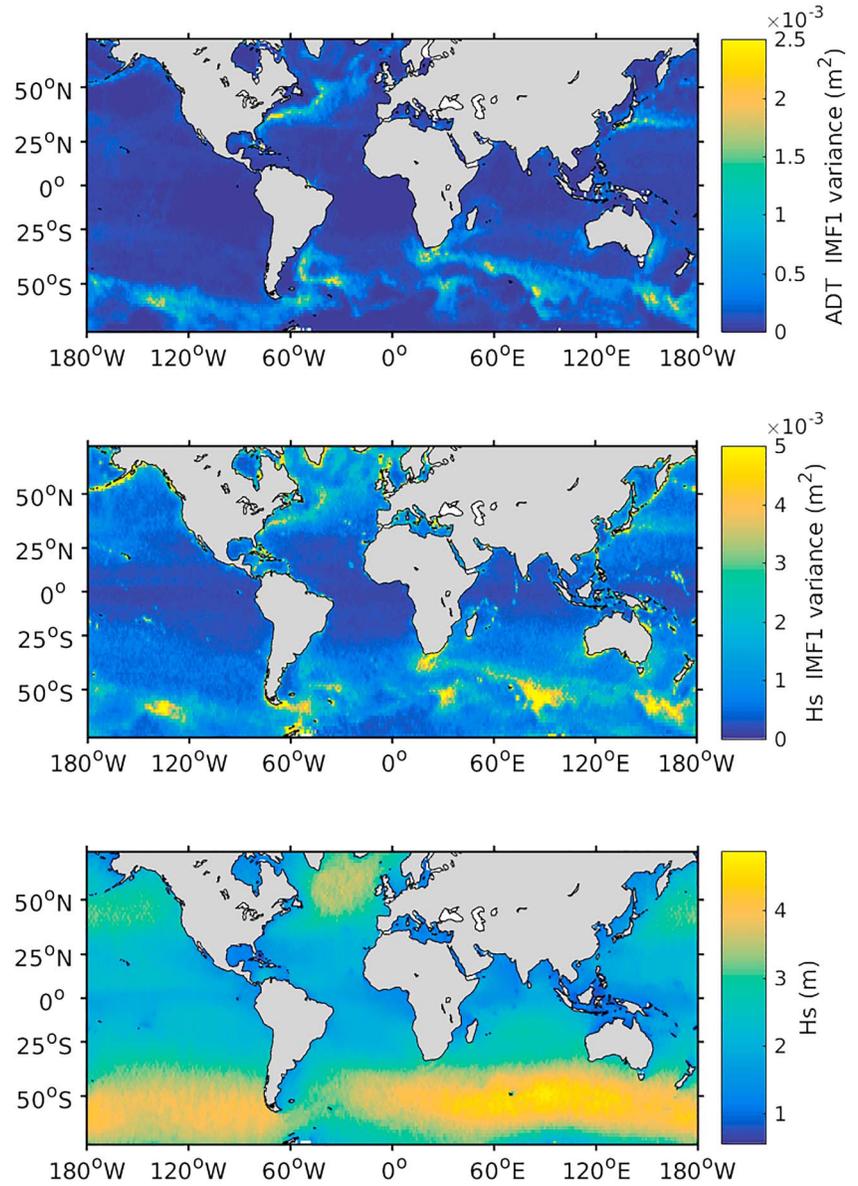
Figure 2. Mean variance field of the first IMF of denoised ADT (top panel) and Hs (middle panel) data, and corresponding mean total Hs field (bottom panel). Mean estimates are computed on a 1° × 1° longitude/latitude grid using the three altimeters data from 2014 to 2016.

$$d\mathbf{x}/dt = \frac{\partial \Omega}{\partial \mathbf{k}} \tag{1}$$

$$d\mathbf{k}/dt = -\frac{\partial \Omega}{\partial \mathbf{x}} \tag{2}$$

$$dN/dt = 0 \tag{3}$$

where $\Omega(\mathbf{k}, \mathbf{x}) = \sqrt{gk} + \mathbf{k} \cdot \boldsymbol{u}$ is the dispersion function, $N(\mathbf{k}) = E(\mathbf{k})/\sqrt{gk}$ is the wave action, $\mathbf{k}$ is the wave vector, and $\mathbf{u}$ is the surface current vector. Bold characters designate vectors.

Rays along which the swell train propagates in the variable current field can be computed by numerically solving for the first two equations. Details are given in Kudryavtsev et al. (2017) and Quilfen et al. (2018). The resulting ray tracing analysis can appropriately portray the modified propagation paths and resulting
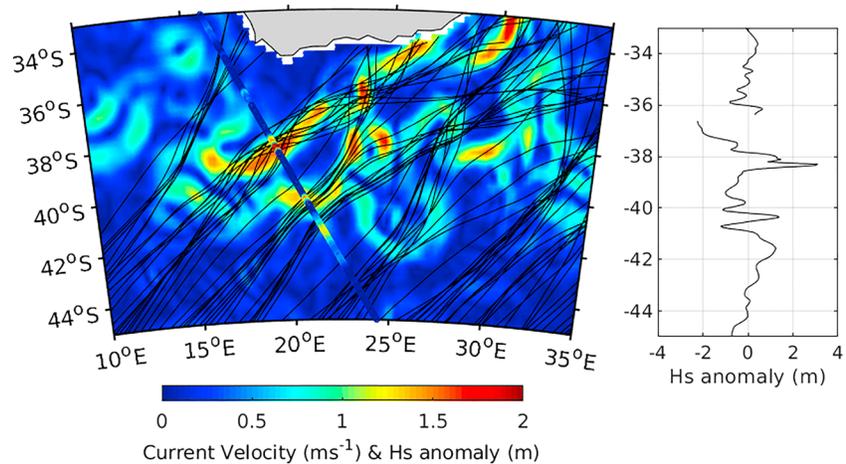
Figure 3. Surface current velocity (left panel) on 28 February 2016 and superimposed swell rays (solid black lines). Jason-2 Hs anomalies (cycle 282, pass 46) are shown on both the left panel (color-coded) and the right panel (*x* axis in m/s) as a function of latitude (*y* axis). Hs anomalies are the denoised Hs whose along-track trend has been removed.

energy focus. These results are used in the following section to explain the observed sea state variability in the Agulhas current region.

3.2. Observed Wave Height Anomalies and Wave/Current Interactions in the Agulhas Region

Figure 3 shows a particular case of a far-field storm swell that was generated in the southwest of the Agulhas area at the end of February 2016 with a 460-m peak wavelength and an incoming angle of 50° relative to north. The waves traveled for almost 2 days, 28 to 29 February, with a group velocity of more than 13 m/s through the Agulhas current system. The surface current peaks near 2 m/s. To leading order, the direction of propagation will be deflected by an angle $\theta = \xi l / V_g$, where ξ is the current vorticity, l is the distance, and V_g is the wave group velocity (Dysthe, 2001). A swell with a wavelength of 460 m that travels over a distance of 200 km in a current with a mean vorticity of 2×10^{-5} s^{-1} will thus be deflected by an angle of approximately 17°. The left panel of Figure 3 shows that predicted rays indeed bend to possibly redistribute the initial energy randomly (as compared to a standard wave propagation front).

A Jason-2 altimeter pass intersected the area on 29 February, crossing different parts of the Agulhas current system at a time when the swell train was still traveling through the area (as observed from the European Space Agency Sentinel-1 Synthetic Aperture Radar and the WAVEWATCH III numerical model, not shown). The right plot in Figure 3 shows the along-track Hs anomalies as a function of latitude. Two positive anomalies associated with very large Hs gradients are located near −38.3° and −40.3° of latitude at locations where swell rays are shown to converge, certainly focusing energy. The Hs values associated with these anomalies are close to 9 and 6 m. Such large Hs values and gradients are associated with dangerous sea state conditions with steep waves, and the prediction of such conditions remains a challenge for state-of-the-art numerical models. As shown in Figure 3, the role of the main Agulhas current branch flowing southwestward apparently becomes a wave guide, as the opposing and refracted swell will be trapped in the center of the current jet (Lavrenov & Porubov, 2006). As a result of the conservation of wave action, equation (3) in the previous section, swell focusing results in locally accumulated wave energy, which is in agreement with the altimeter Hs measurements. Rays convergences and divergences are shown in the vicinity of the Agulhas Return Current, where eddies further add complexity to the ray patterns. Locations where the ray density is low also correspond to low sea state conditions. This condition is adequately caught by the altimeter between the two Hs peaks and north of the main 9-m Hs peak.

This particular case study thus illustrates the expected sea state variability resulting from wave/current interactions. More statistical results are presented in Figure 4. The Agulhas region is an avenue for swells generated in southern latitudes by storms (see supporting information, Figure S4). Statistically, 88% of the peak wave directions are located in the southwest quadrant, with a clearly marked unimodal distribution at 230°, indicating prevailing northeastward wave propagation. Associated wavelengths vary from 100 to
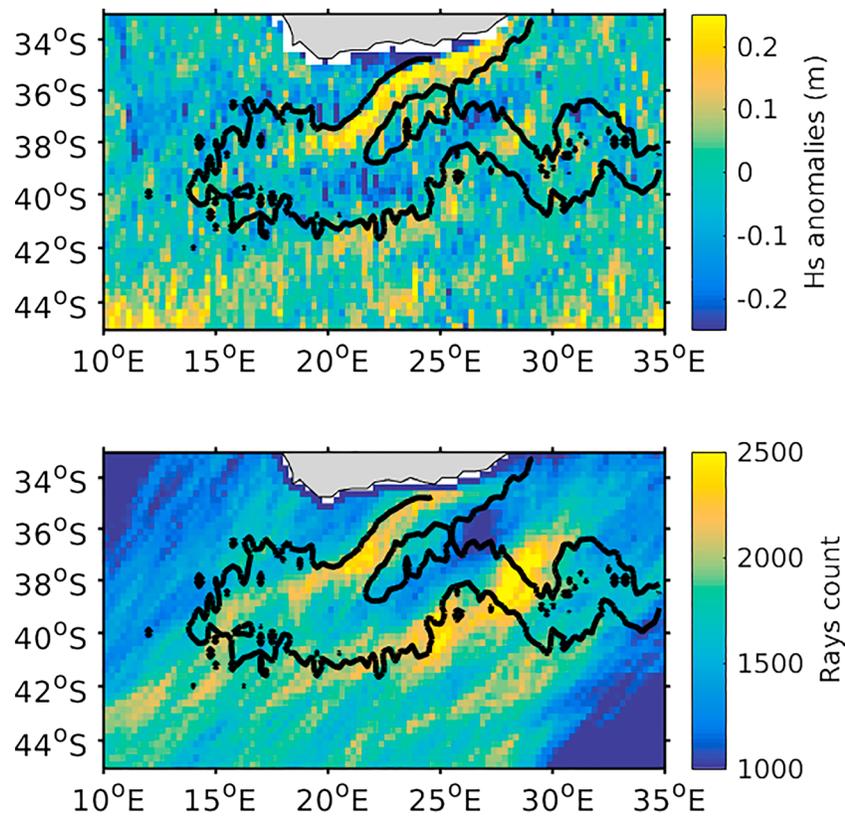
Figure 4. Mean values (2014–2016) in a 0.25° × 0.25° grid of Hs anomalies (top) and mean number of swell rays (bottom). Swell rays are generated for a random Gaussian distribution of swells coming from the southwest corner of the area with a given wavelength of 250 m and varying directions with a mean and standard deviation of 52° (clockwise relative to north) and 13°, respectively. The solid black line indicates the 0.5 m/s isocontour of mean surface current velocity.

500 m. The top panel of Figure 4 shows mean Hs anomalies in the Agulhas region from 2014 to 2016, which were computed at each cell of a 1/4° resolution grid. Hs anomalies are computed by detrending the denoised Hs data along each segment of orbit crossing the area. The lower panel of Figure 4 shows mean density of rays, which was computed for a Gaussian distribution of sea state conditions at the boundary of the domain, best approaching the one obtained via WAVEWATCH III predictions (see supporting information, Figure S4). For the ray density, the number of rays was calculated for each cell and every day over 2014–2016. For each day, the daily CMEMS current field has been used to predict the ray field, as illustrated in Figure 3, for a wave train with the swell direction randomly drawn from the Gaussian distribution. This result then approaches a realistic framework for comparisons with the distribution of Hs anomalies.

No spatial smoothing/interpolation was applied to the mean Hs anomaly field, but again, clear patterns of higher and lower values emerged. In particular, the Hs values are large in the southwestward flowing Agulhas branch and low in the northeastward flowing branch. These locations are where the main surface current flow is rather regular. The ray density map further shows evidence of high and low ray densities, and these results are consistent with the conceptual modeling of wave energy transformation by current gradients. In other locations, the ray density patterns are less delineated in areas that have more eddies.

4. Discussion and Conclusions

Surface currents have long been shown to impact sea state (Lavrenov & Porubov, 2006; Mallory, 1974; White & Fornberg, 1998). Using an approach that combined numerical modeling of the wavefield and satellite altimeter measurements, Ardhuin et al. (2017) analyzed a few regional cases. Although a relationship was proposed between the mesoscale Hs variability predicted by the WAVEWATCH III numerical model and the

surface currents used to trigger the model, comparisons with altimeter measurements were not as conclusive. This is because the mesoscale geophysical variability is strongly buried within altimeter measurement noise, impacting scales up to 100 km.

Here a self-consistent space-scale decomposition has been applied. As demonstrated, the methodology self-adjusts to different altimeter instruments and best removes the specific instrumental noise from different altimeters. This method then helps to map overlooked statistical properties at scales less than 100 km, where mesoscale and submesoscale upper ocean circulation drives a significant part of the coupled ocean/atmosphere system variability.

The resulting yearly mean signal variance (amplitude squared), as mapped over the global oceans and shown in Figure 2, indeed shows that both ADT and Hs variability patterns closely coincide over highly dynamical oceanic regions. This result supports the findings of previous case studies (e.g., Ardhuin et al., 2017; Kudryavtsev et al., 2017; Quilfen et al., 2018).

As further analyzed in the Agulhas current region, a dominant regime of incoming southwesterly waves imprints the local wave climatology. Persistent patterns clearly result from the cumulative impacts of the large-scale and persistent nature of the current vorticity field on wave train kinematics. Because of the significant ray deflection and trapping phenomena, localized sea state gradients can be anticipated and are well traced in altimeter signals. The ray tracing analysis performed over a 3-year time period explains the link between observed climatological sea state anomaly patterns and the Agulhas current patterns. As ray transformation is a first-principle physical phenomenon, the Agulhas results should apply to other regions highlighted in Figure 1, and also corroborate the Ardhuin et al. (2017) study.

Building on the long-range propagation of ocean swells (Collard et al., 2009; Delpey et al., 2010; Li, 2016), altimeter signals have great potential to assess refraction effects, improve wave forecasts and comparisons with other (satellite, in situ) sea state measurements, as well as separate persistent and more random small-scale wave-current interactions. The continuing altimeter data record, combined with the upcoming Surface Water and Ocean Topography, China-France Oceanography Satellite, and foreseen Sea Surface Kinematics Multiscale Monitoring missions, should thus further contribute to an improved understanding of the nature of both the spatial and temporal variability of these distributed statistical properties and of the possible dynamic impacts of the coupling between waves and surface currents.

References

Ardhuin, F., Gille, S. T., Menemenlis, D., Rocha, C. B., Rascle, N., Chapron, B., et al. (2017). Small-scale open-ocean currents have large effects on wind-wave heights. *Journal of Geophysical Research: Oceans*, *122*, 4500–4517. https://doi.org/10.1029/2016JC012413

Carmona, A., & Poveda, G. (2014). Detection of long-term trends in monthly hydro-climatic series of Colombia through empirical mode decomposition. *Climatic Change*, *123*(2), 301–313. https://doi.org/10.1007/s10584-013-1046-3

Chen, X., Zhang, X., Church, J. A., Watson, C. S., King, M. A., Monselesan, D., et al. (2017). The increasing rate of global mean sea-level rise during 1993–2014. *Nature Climate Change*, *7*(7), 492–495. https://doi.org/10.1038/nclimate3325

Chen, X., Zhang, Y., Zhang, M., Feng, Y., Wu, Z., Qiao, F., & Huang, N. E. (2013). Intercomparison between observed and simulated variability in global ocean heat content using empirical mode decomposition. Part I: Modulated annual cycle. *Climate Dynamics*, *41*(11-12), 2797–2815. https://doi.org/10.1007/s00382-012-1554-2

Collard, F., Ardhuin, F., & Chapron, B. (2009). Monitoring and analysis of ocean swell fields from space: New methods for routine observations. *Journal of Geophysical Research*, *114*, C07023. https://doi.org/10.1029/2008JC005215

Delpey, M. T., Ardhuin, F., Collard, F., & Chapron, B. (2010). Space-time structure of long ocean swell fields. *Journal of Geophysical Research*, *115*, C12037. https://doi.org/10.1029/2009JC005885

Dibarboure, G., Boy, F., Desjonqueres, J. D., Labroue, S., Lasne, Y., Picot, N., et al. (2014). Investigating short-wavelength correlated errors on low-resolution mode altimetry. *Journal of Atmospheric and Oceanic Technology*, *31*(6), 1337–1362. https://doi.org/10.1175/JTECH-D-13-00081.1

Ducet, N., Le Traon, P. Y., & Reverdin, G. (2000). Global high-resolution mapping of the ocean circulation from TOPEX/POSEIDON and ERS-1/2. *Journal of Geophysical Research*, *105*(C8), 19,477–19,498. https://doi.org/10.1029/2000JC900063

Dufau, C., Orsztynowicz, M., Dibarboure, G., Morrow, R., & Le Traon, P. Y. (2016). Mesoscale resolution capability of altimetry: Present and future. *Journal of Geophysical Research: Oceans*, *121*, 4910–4927. https://doi.org/10.1002/2015JC010904

Dysthe, K. (2001). Refraction of gravity waves by weak current gradients. *Journal of Fluid Mechanics*, *442*, 157–159. https://doi.org/10.1017/S0022112001005237

Flandrin, P., Rilling, G., & Goncalves, P. (2004). Empirical mode decomposition as a filter bank. *IEEE Signal Processing Letters*, *11*(2), 112–114. https://doi.org/10.1109/LSP.2003.821662

Gallet, B., & Young, W. R. (2014). Refraction of swell by surface currents. *Journal of Marine Research*, *72*(2), 105–126. https://doi.org/10.1357/002224014813758959

Han, J., & van der Baan, M. (2015). Microseismic and seismic denoising via ensemble empirical mode decomposition and adaptive thresholding. *Geophysics*, *51*(12), 2247–2249. https://doi.org/10.1190/1.1442078

Heslop, E. E., Sánchez-Román, A., Pascual, A., Rodríguez, D., Reeve, K. A., Faugère, Y., & Raynal, M. (2017). Sentinel-3A views ocean variability more accurately at finer resolution. *Geophysical Research Letters*, *44*, 12,367–12,374. https://doi.org/10.1002/2017GL076244

Huang, N. E., Shen, Z., Long, S. R., Wu, M. C., Shih, H. H., Zheng, Q., et al. (1998). The empirical mode decomposition and the Hilbert spectrum for nonlinear and non-stationary time series analysis. *Proceedings of the Royal Society of London*, *454*(1971), 903–995. https://doi.org/10.1098/rspa.1998.0193

Huang, N. E., & Wu, Z. (2008). A review on Hilbert-Huang transform: Method and its applications to geophysical studies. *Reviews of Geophysics*, *46*, RG2006. https://doi.org/10.1029/2007RG000228

Irvine, D. E., & Tilley, D. G. (1988). Ocean wave directional spectra and wave-current interaction in the Agulhas from the shuttle imaging radar-B synthetic aperture radar. *Journal of Geophysical Research*, *93*(C12), 15,389–15,401. https://doi.org/10.1029/JC093iC12p15389

Kenyon, K. E. (1971). Wave refraction in ocean currents. *Deep Sea Research and Oceanographic Abstracts*, *18*(10), 1023–1034. https://doi.org/10.1016/0011-7471(71)90006-4

Kopsinis, Y., & McLaughlin, S. (2009). Development of EMD-based denoising methods inspired by wavelet thresholding. *IEEE Transactions on Signal Processing*, *57*(4), 1351–1362. https://doi.org/10.1109/TSP.2009.2013885

Kudryavtsev, V., Yurovskaya, M., Chapron, B., Collard, F., & Donlon, C. (2017). Sun glitter imagery of surface waves. Part 2: Waves transformation on ocean currents. *Journal of Geophysical Research: Oceans*, *122*, 1384–1399. https://doi.org/10.1002/2016JC012426

Lavrenov, I. V., & Porubov, A. V. (2006). Three reasons for freak wave generation in the non-uniform current. *European Journal of Mechanics - B/Fluids*, *25*(5), 574–585. https://doi.org/10.1016/j.euromechflu.2006.02.009

Li, X.-M. (2016). A new insight from space into swell propagation and crossing in the global oceans. *Geophysical Research Letters*, *43*, 5202–5209. https://doi.org/10.1002/2016GL068702

Mallory, J. K. (1974). Abnormal waves in the south-east coast of South Africa. *International Hydrographic Review*, *51*, 89–129.

Morrow, R., Carret, A., Birol, F., Nino, F., Valladeau, G., Boy, F., et al. (2017). Observability of fine-scale ocean dynamics in the Northwest Mediterranean Sea. *Ocean Science*, *13*(1), 13–29. https://doi.org/10.5194/os-13-13-2017

Queffeulou P., & Croizé-Fillon, D. (2013). Global altimeter Hs data set, version 10. Laboratoire d'Océanographie Spatiale, IFREMER, Z.I. de la Pointe du Diable, CS10070, 29280 Plouzané, France.

Quilfen, Y., Yurovskaya, M., Chapron, B., & Ardhuin, F. (2018). Storm waves focusing and steepening in the Agulhas current: Satellite observations and modeling. *Remote Sensing of Environment*, *216*, 561–571. https://doi.org/10.1016/j.rse.2018.07.020

Sandwell, D. T., & Smith, W. H. F. (2005). Retracking ERS-1 altimeter waveforms for optimal gravity field recovery. *Geophysical Journal International*, *163*(1), 79–89. https://doi.org/10.1111/j.1365-246X.2005.02724.x

Thibaut, P., Poisson, J. C., Bronner, E., & Picot, N. (2010). Relative performance of the MLE3 and MLE4 Retracking algorithms on Jason-2 altimeter waveforms. *Marine Geodesy*, *33*(sup1), 317–335. https://doi.org/10.1080/01490419.2010.491033

Wang, W., Chau, K., Qiu, L., & Chen, Y. (2015). Improving forecasting accuracy of medium and long-term runoff using artificial neural network based on EEMD decomposition. *Environmental Research*, *151*, 30–37. https://doi.org/10.1016/j.envres.2016.07.002

White, B. S., & Fornberg, B. (1998). On the chance of freak waves at sea. *Journal of Fluid Mechanics*, *355*, 113–138. https://doi.org/10.1017/S002211209700775

Wu, Z., & Huang, N. E. (2004). A study of the characteristics of white noise using the empirical mode decomposition method. *Proceedings of the Royal Society of London*, *460*(2046), 1597–1611. https://doi.org/10.1098/rspa.2003.1221

Xu, X., Chassignet, E. P., Johns, W. E., Schmitz, W. J., & Metzger, E. J. (2014). Intraseasonal to interannual variability of the Atlantic meridional overturning circulation from eddy-resolving simulations and observations. *Journal of Geophysical Research: Oceans*, *119*, 5140–5159. https://doi.org/10.1002/2014JC009994